Influence of microstructure on the mechanical behavior of open-porous materials under large strains

Rajesh Chandrasekaran [a],*, Mikhail Itskov [a], Ameya Rege [b]

[a] *Department of Continuum Mechanics, RWTH Aachen University, Eilfschornsteinstr. 18, Aachen, 52062, Germany*
[b] *Department of Mechanics of Solids, Surfaces & System, University of Twente, PO Box 217, 7500 AE, Enschede, Netherlands*

ARTICLE INFO

ABSTRACT

Open-porous materials are characterized by a complex morphology consisting of an interconnected solid network and voids. The mechanical performance of these materials is strongly governed by their underlying microstructure. This study presents a computational framework to investigate the structure–property relationships in open-porous materials by explicitly modeling the effects of pore-size distribution (PSD), solid fraction, and pore wall geometry. Microstructures with tunable PSDs are generated using Laguerre-Voronoi tessellation based on random closed packing of polydisperse spheres, allowing precise control over pore morphology. A finite element framework with the elastoplastic material model is used to study the macroscopic behavior under compressive loading. The model response is validated against experimental data from aerogel and foam materials. The study reveals that while the solid fraction alone governs the bulk elastic modulus and plastic collapse stress through well-established scaling laws, the PSD critically affects the post-yield behavior, including the plateau and densification regimes under large strains. This study highlights the importance of PSD beyond classical density-based models and provides a predictive design strategy to tailor open-porous materials to application-specific mechanical requirements.

1. Introduction

Due to depleting resources, rising cost of raw materials, and advancements in sustainability, reducing material consumption in automotive, aerospace, and machinery has become an ongoing challenge. Therefore, there is an increasing demand for the development of lightweight and multifunctional innovative materials with enhanced mechanical and thermal properties. One of the promising classes of materials for light-weight design and multifunctional applications are porous materials, which consist of an interconnected solid structure surrounding a network of pores, offering high structural rigidity and low mass density. While natural and synthetic open-porous materials have been investigated for several decades, open-porous nanomaterials have seen a rise in advancements over the past decade. Nanoporous materials typically have pore-sizes in the range of 2 to 100 nm and exhibit fascinating mechanical and thermal properties, such as ultralow density, high energy absorption capacity, better thermal management, and excellent durability under dynamic loading conditions (Thommes and Schlumberger, 2021; Merillas et al., 2022). Typical examples of nanoporous solids are zeolites, activated carbon, metal–organic frameworks and aerogels (Polarz and Smarsly, 2002).

In recent decades, research on the synthesis, characterization, functionalization, molecular modeling, and design of new and novel nanoporous materials has witnessed an exponential rise due to their increasing demand in a wide spectrum of applications (Davis, 2002; Kelly, 2006; Smith et al., 2012; Bennett et al., 2021; Ates et al., 2022). Porous materials can be synthesized using various fabrication techniques such as foaming, precipitation, solid state reaction (usually performed at high temperature), sol–gel, hydrothermal, and solvothermal synthesis routes (Yang et al., 2017; Rechberger and Niederberger, 2017; Zhao et al., 2018; Jin et al., 2019; Cai et al., 2021). By exploring different materials to form the skeletal backbone for designing the solid network with different pore morphologies, we can achieve a unique and attractive combination of their mechanical and thermal properties. The structure, pore-size and subsequently the pore fraction, specific surface area and density of nanoporous materials could be tailored using different fabrication techniques. To this end, the characterization of the structure–property relationship of such materials is key to their material design. They are typically characterized by two essential microstructural features, namely density and pore-size distribution (PSD). Density is often interpreted in terms of the dimensionless quantity,

---

termed relative density, which is the ratio of the envelope density (ρ_e) to the skeletal density (ρ_s). This is directly related to the solid fraction ($\phi_s = \rho_e/\rho_s$) of the structure. The PSD characterizes the relative abundance of each pore-size in a representative volume of the material. Both microstructural parameters, ϕ_s and PSD, can be measured experimentally using various characterization techniques.

Open-porous materials, including nanoporous types, are widely used across different fields such as energy absorbers in crash, scaffolds in tissue engineering, carrier materials for drugs, food packaging and other applications that demand a stable mechanical performance with insulating properties. Some of these materials show brittle behavior in tension and undergo elastoplastic deformation under large strains in compression. On the other hand, there also exist highly flexible materials that undergo large reversible deformations. Most tests on cellular-like nanoporous materials are performed under compressive loading, where significant energy absorption can be observed. Under monotonic loading, the typical behavior of porous materials is characterized by three major phenomena that give rise to the resulting deformation zones: (a) a small elastic regime, where the pore walls undergo elastic bending and buckling, followed by (b) a plateau regime which results from plastic yielding and pore collapse, and (c) the densification regime with a rapid increase in peak stress under a considerably small increase in strain (Rege, 2021), where the collapsed pores begin to densify resulting in hardening of the network. Under cyclic loading, open-porous materials show inelastic behavior with a hysteresis cycle and residual deformations (Santos-Rosales et al., 2020).

The main challenge remains the correlation of the structural features with the mechanical properties to enable reverse engineering through optimization techniques. In comparison to trial-and-error laboratory experiments, numerical modeling and computer simulation is a cost- and resource-efficient method to study such structure–property relationships. Gibson and Ashby (Gibson et al., 1982; Gibson and Ashby, 1982) expressed the mechanical properties such as Young's modulus and compressive strength in the form of power laws with respect to the densities in porous materials. Besides, the micromechanically motivated constitutive model recently developed by Rege et al. (2021) has shown good predictive capabilities in describing the mechanical behavior of aerogel materials. While these models account for the PSD, they tend to ignore the heterogeneous morphology of the pore structure in terms of its shape. The PSD solely describes the spatial variation of the pore-sizes and has recently been shown to influence the mechanical properties of porous materials (Rege et al., 2021; Aney and Rege, 2023). These open-porous materials can be designed computationally using models that inherit the most important geometric properties, such as the solid fraction and the PSD. The most widely used computational methods for reconstructing the porous structure are Voronoi tessellations. Kraynik (2006) as well as Ghosh and Moorthy (2004) have demonstrated the application of 3-d Voronoi tessellations to describe the porous architecture of foam-like materials. Several other authors have extended these studies and validated the use of Voronoi-based approaches to accurately describe the mechanical and thermal properties of foam-like porous materials (Sotomayor and Tippur, 2014; Sharma et al., 2019; Aney and Rege, 2025). Recently, with the aim of accounting for the polydispersity in the pore sizes, Chandrasekaran et al. (2021) reconstructed the 3-d nanoporous microstructure of biopolymer aerogels using Laguerre-Voronoi tesselation (LVT) based on random closed packing of polydisperse spheres (RCPPS). This model approach requires PSD and solid fraction to adequately represent the 3-d nanoporous morphology of the material, while still proving to be accurate in predicting the bulk macroscopic behavior.

While a few studies have demonstrated the application of elastoplastic models within the Voronoi framework, to the best of our knowledge, investigations on the influence of the geometric parameters on the large deformation behavior, particularly the densification in open-porous materials, have not yet been reported. The present work is motivated by the larger goal of understanding the structure–property

relations to guide and optimize the synthesis of open-porous materials. This can be achieved by correlating the synthesis characteristics with model parameters as shown in Rege et al. (2018). To this end, the article presents the computational studies on the influence of different geometric parameters on the bulk mechanical response under large deformations using the framework proposed in Chandrasekaran et al. (2021). The elastic and inelastic response of various open-porous structures with PSD based on different probability density functions (PDFs) and different combinations of other geometric properties is studied. Geometric properties that are interdependent and more sensitive to the bulk response are identified.

2. Methods

This section discusses the method of determining the PSD for a given choice of PDF, namely beta, log-normal or normal distribution. This choice of PDFs is in line with experimental observations in polydisperse nanoporous materials (Rege et al., 2016). In addition, an overview of geometric and finite element (FE) modeling based on the given probability is elaborated.

Generally, regardless of the experimental methodology, the PSD is derived by stepwise determination of pore volume increments for corresponding pore-width intervals. Accordingly, the sum of all the pore volume increments represents the total pore volume. Since spherical pores are assumed for the following study, the pore-width can be expressed by the pore diameter D. The PSD is represented by a function $P(D)$ proportional to the combined volume of all pores whose effective pore diameter lies within an infinitesimal range centered on D. Hence, the PSD can be obtained from the ratio of the pore volume increment ΔV_i for each pore-width D_i and the total pore volume as

$$P(D_i) = \frac{\Delta V_i}{\sum_{j=1}^{n} \Delta V_j}, \tag{1}$$

where n is the total number of pore-width intervals.

The cumulative PSD (P_c) can be obtained from the ratio of the partial sums of the pore volume increment, i.e., that of the cumulative pore volume to the total pore volume as

$$P_c(D_i) = \frac{\sum_{k=1}^{i} \Delta V_k}{\sum_{j=1}^{n} \Delta V_j}. \tag{2}$$

2.1. Determination of pore-size distribution (PSD) from probability density function (PDF)

The equivalent PSD is determined from the PDF for a given set of pore-diameter intervals D and binwidth dD. The set of pore-diameter intervals is represented as $D = \{D_i\}$ with $i = 1, 2, 3, \ldots, n$.

The volume of each pore with diameter D_i can be expressed by

$$V_i = f_1(D_i). \tag{3}$$

Further, the number of pores with the diameter between D_i and $D_i + dD$ takes the form

$$dN_i = N f_2(D_i) dD. \tag{4}$$

where f_2 is the probability density function and N is the total number of pores in a system.

The volume of all pores with the diameter between D_i and $D_i + dD$ can thus be written as

$$dV_i = V_i dN_i = N f_1(D_i) f_2(D_i) dD. \tag{5}$$

The theoretical PSD can be obtained from the ratio of the volume of all pores with diameters between D_i and $D_i + dD$ to the total pore volume in the system as

$$P(D_i) = \frac{dV_i}{\sum_{j=1}^{n} dV_j} = \frac{f_1(D_i) f_2(D_i)}{\sum_{j=1}^{n} f_1(D_j) f_2(D_j)}. \tag{6}$$
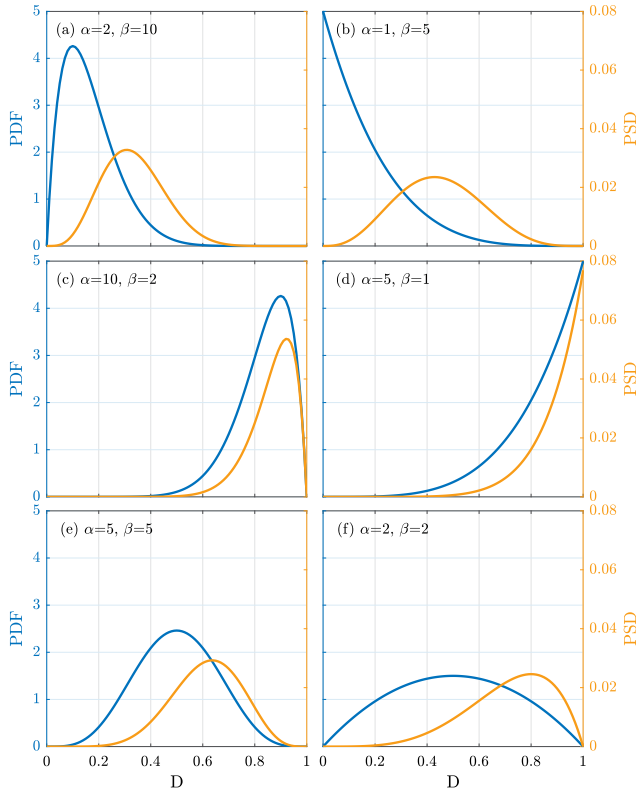
Fig. 1. Comparison between the PDF and PSD for beta distribution with different skewness: (a) & (b) Right-skewed ($\alpha < \beta$), (c) & (d) Left-skewed ($\alpha > \beta$), and (e) & (f) Symmetric ($\alpha = \beta$).

The theoretical cumulative PSD can be obtained from the ratio of the sum of the volumes of all pores with a diameter up to D_i to the total volume of all pores in the system as

$$P_c(D_i) = \frac{\sum_{k=1}^{i} dV_k}{\sum_{j=1}^{n} dV_j} = \frac{\sum_{k=1}^{i} f_1(D_i) f_2(D_i)}{\sum_{j=1}^{n} f_1(D_j) f_2(D_j)}. \tag{7}$$

In order to solve Eq. (3) & (4), it is necessary to obtain the explicit functions f_1 and f_2, which depend on the geometrical type of the pore model as follows.

- For a spherical type pore model, $f_1(d) = \frac{\pi}{6} d^3$, where d is the diameter of the spherical pore.
- For a cylindrical type pore model, $f_1(d) = \frac{\pi}{4} l d^2$, where d is the diameter and l is the length of the cylindrical pore.
- For the beta distribution,
  $f_2(x) = \frac{\Gamma(\alpha+\beta)}{\Gamma(\alpha)\Gamma(\beta)} \cdot x^{\alpha-1} \cdot (1-x)^{\beta-1}$, where

  - x is the pore diameter in the interval $[0, 1]$,
  - α and β are the shape parameters,
  - Γ is a gamma function.

- For the normal distribution,
  $f_2(x) = \frac{1}{s\sqrt{2\pi}} e^{-\frac{1}{2}\left(\frac{x-\mu}{s}\right)^2}$, where

  - x is the pore diameter, i.e., $x \in \mathbb{R}$,
  - μ is the mean,
  - s is the standard deviation.

- For the log-normal distribution,
  $f_2(x) = \frac{1}{xs\sqrt{2\pi}} e^{-\frac{1}{2}\left(\frac{\ln x-\mu}{s}\right)^2}$, where

- x is the pore diameter in the interval $[0, +\infty]$,
- μ is the mean of the natural logarithm of the variable in the interval $[-\infty, +\infty]$,
- s standard deviation of the natural logarithm of the variable, i.e., $s > 0$.

The comparison between the probability density function and the corresponding PSD is illustrated in Fig. 1 using a beta distribution for different shape parameters α and β and assuming the pore shape to be spherical. It is observed that the contribution of the larger pores is dominant in the PSD, although the occurrence probability of the smaller pores is higher. In Fig. 1, a right-skewed PDF shows a symmetric PSD, and a symmetric PDF shows a left-skewed PSD. Thus, one should not misinterpret PSD as PDF and vice versa. This can lead to completely different analysis and interpretation.

2.2. Modeling of the open-porous network

This section discusses the geometric and finite element (FE) modeling of the porous structure using symmetric beta PDF with $\alpha = 5$ & $\beta = 5$ (hereafter referred to as reference PDF). A computational model of a porous structure with highly dispersed pore-sizes can be created using a random closed packing of polydisperse spheres (RCPPS) and Laguerre-Voronoi tessellation (LVT). This combined technique has been shown to be a powerful method to computationally generate and model porous materials (Chandrasekaran et al., 2021).

2.2.1. Geometric modeling

In the modeling of porous structures, the following geometric properties have to be considered: porosity/solid fraction/relative density and PSD, which are the essential input parameters for the generation of the microstructure. In general, Voronoi tessellation is capable of representing the microstructure of porous materials with an interconnected network structure. However, it limits the control over the PSD due to the randomized spatial distribution of seed points in 3-d space and the generation of cell boundaries equidistant between seed points. LVT is a weighted version of Voronoi tessellations, where the pore-sizes can be controlled by defining specific weights for each seed. The resulting position of the seed in the 3-d space and the corresponding weights required for LVT are provided by RCPPS as sphere centers and radii, respectively. Consequently, a periodic 3-d structure capturing a particular PSD with an interconnected solid network is generated. Although LVT is initially performed under the assumption of spherical pores as a consequence of the RCPPS algorithm, the resulting pore shapes within the generated microstructure exhibit irregular geometries. In addition to the PSD, a microstructure model with a given solid fraction can be obtained by defining appropriate cross-sectional properties to the cell walls of the Voronoi structure.

In this study, the cell walls of the porous structure are assumed to be cylindrical. Consequently, an appropriate cell wall diameter (CWD) must be determined to obtain the desired solid fraction. This can be achieved by using one of the following approaches: (1) **Constant diameter (CD) approach**: a constant CWD is defined throughout the structure to maintain a constant porosity throughout the model. (2) **Diameter distribution (DD) approach**: a distinct diameter is assigned to each cell wall, ensuring a constant porosity for each individual pore within the structure. The CD method provides a structure with distinct porosity for each pore but has a constant CWD throughout. In contrast, the latter method provides a structure with constant porosity at the pore level, but a distinct CWD (for more details see Chandrasekaran et al., 2021).

The generation of a computational microstructure model with pore sizes ranging from 5 to 100 nm and a porosity of 95% ($\phi_s = 0.05$) for the reference PDF is illustrated in Fig. 2. Based on the desired PSD (Fig. 2(a)) and the total number of pores (N) in the porous system,
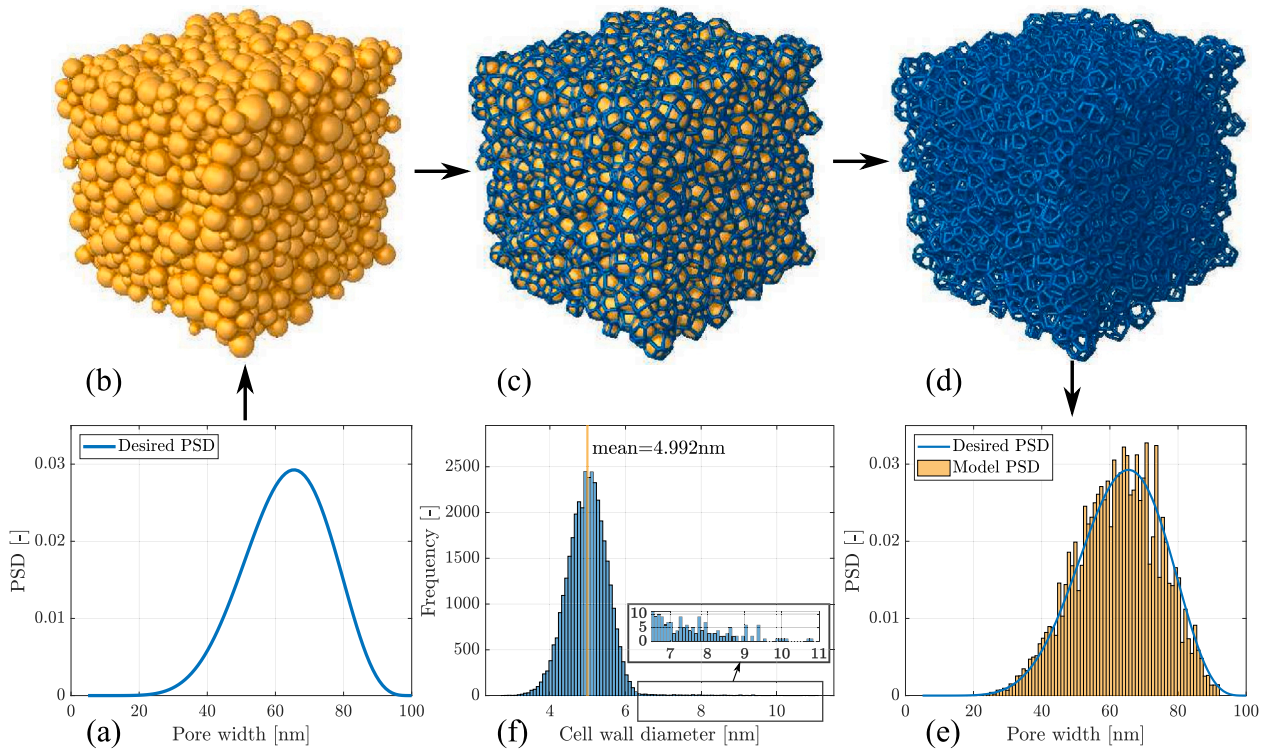
Fig. 2. Model workflow using RCPPS and LVT: (a) Desired PSD corresponding to reference PDF for N=3000 (b) RCPPS, (c) LVT, (d) Microstructure model, and (e) Comparison of desired PSD with the PSD of resulting microstructure model, (f) CWD for a given solid fraction of 0.05, illustrating CD (mean) and DD (histogram) approaches.

the size of the packing domain is determined and provided as input to the sphere packing algorithm. The coordinates of the centers and the corresponding radii of the packed spheres are then given as input to the LVT algorithm (Fig. 2(b)). LVT based on RCPPS is illustrated in Fig. 2(c). The microstructure model with the desired properties is shown in Fig. 2(d). The PSD of the generated structure is compared to the desired input PSD, shown as a histogram in Fig. 2(e). For the given solid fraction of 0.05, the distribution of CWD determined using the DD approach and the average CWD obtained using the CD approach are presented in Fig. 2(f).

2.2.2. FE modeling

The Voronoi diagram generated in the geometric modeling is transformed into a cubic representative volume element (RVE) with periodic boundary conditions (PBCs) as described in Chandrasekaran et al. (2021). The RVE, in conjunction with the PBCs, allows the computation of the homogenized macroscopic response of the material. An example of the RVE of the microstructure model shown in Fig. 2(d), with PBCs, is presented in Fig. 3(a). The cell walls of the Voronoi network are discretized using Hughes–Liu beam elements with circular cross sections. The cross-sectional diameter obtained from the geometric modeling is assigned to the beam elements. A comprehensive description of the RVE generation process can be found in Chandrasekaran et al. (2021). The behavior of the cell walls is modeled using a bilinear elastoplastic material model, as shown in Fig. 3(b). The input parameters for the material model include Young's modulus (E = 4.5 GPa), yield stress (σ_y = 0.1 GPa), and tangent modulus (E_{tan} = 1.0 GPa). The automatic general contact algorithm is used to model the beam-to-beam contact to capture the interaction between cell walls. The model is subjected to monotonic and cyclic compressive loading, and the simulations are performed using the LS-DYNA implicit solver.

3. Results

This section presents the macroscopic response of the microstructure model (RVE) under compression, considering different PSDs, CWDs, and solid fractions.

3.1. Macroscopic response

The RVE of the microstructure, shown in Fig. 3(a), was subjected to cyclic compression up to 70% strain. The corresponding stress–strain response is presented in Fig. 3(c). Contour plots of the von Mises effective stress distribution at 35% and 70% compressive strains are illustrated in Fig. 3(d). The results demonstrate that the RVE model captures both the elastic and inelastic behavior typically observed in such materials (Santos-Rosales et al., 2020). Under compression, the energy is absorbed by the structure as the pore walls (Fig. 3(e)) undergo buckling and bending (Fig. 3(f)). In addition, once the cell walls buckle or bend elastically, the pores begin to collapse, resulting in a plateau in the stress–strain diagram. Subsequently, the collapsed pores resist further deformation due to lack of available space, referred to as densification (Fig. 3(g)). In Fig. 3(c), the linear regime is denoted by the modulus E, and the point where the pore walls undergo plastic deformation is marked as σ_{pl}. Under cyclic loading, the model exhibits behavior similar to the Mullins effect observed in elastomers, characterized by stress softening between the first and subsequent loading, along with a small hysteresis (i.e., the stress softening between the unloading and reloading of the subsequent cycle). The model also captures the permanent set due to the irreversible damage in the microstructure.

The model predictions were validated against experimental data for cellulose aerogels, polyethylene, and aluminium alloy foams available in the literature (Gibson and Ashby, 1999; McCullough et al., 1999; Rege, 2021). To this end, a microstructure model with uniform PSD was generated. The model parameters, specifically ρ_s, E_s and σ_y, were extracted from literatures (Jones and Ashby, 2018; McCullough et al., 1999; Rege, 2021) and summarized in Table 1. E_{tan} was obtained by fitting to the experimental data, and a contact thickness scaling factor between 2 and 3 was used to more accurately capture the densification phase. Fig. 4 shows excellent agreement with experimental results under monotonic and cyclic loading. This confirms that the computational model effectively predicts the macroscopic response of real foam and aerogel materials.
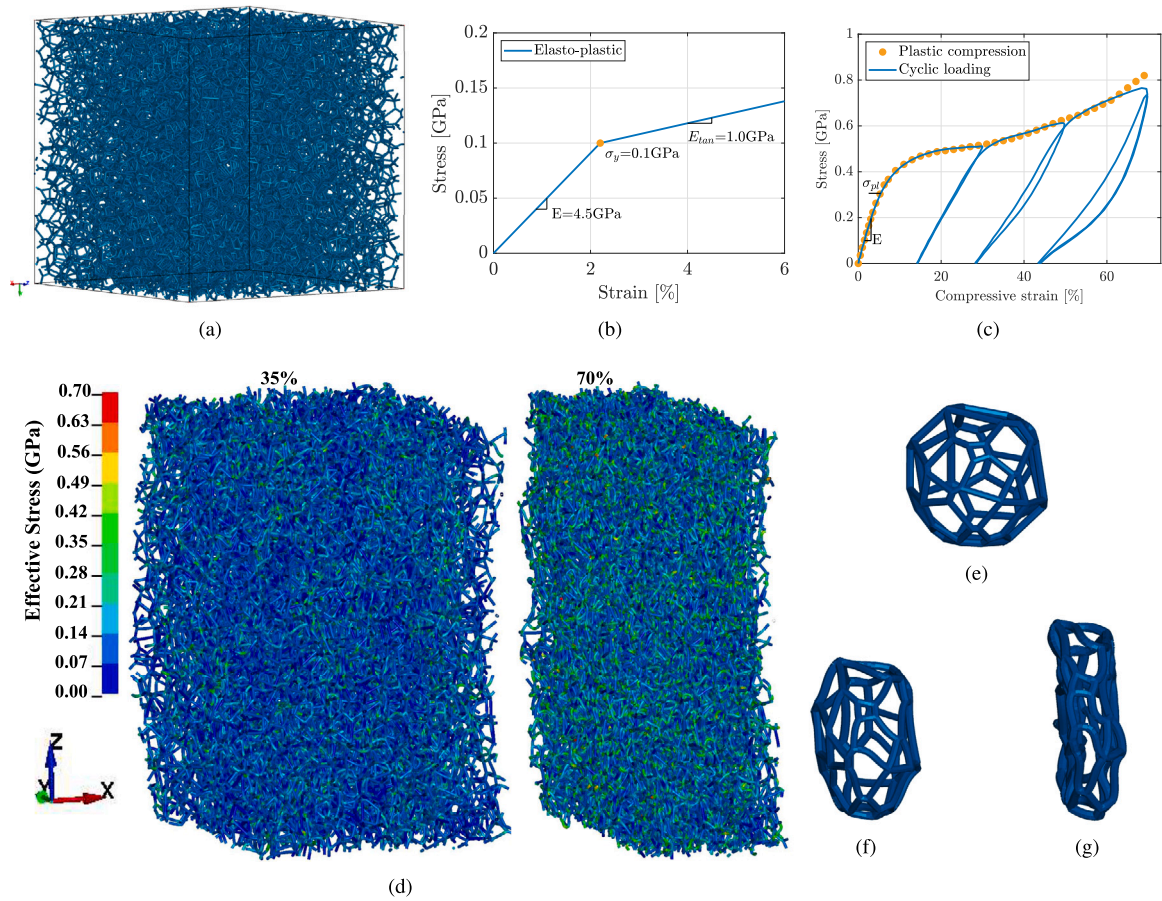
Fig. 3. Illustration of (a) RVE with PBCs, (b) stress–strain diagram of the elastoplastic material model, (c) macroscopic stress–strain response under monotonic and cyclic compressive loading, (d) Von-Misses stress distribution under compression, and illustration of the cell wall behavior due to deformation: (e) undeformed cell, (f) bending and buckling of cell walls, and (g) contact between cell walls after cell collapse.

Table 1
Model parameters for validation.

Materials	ρ_e	ρ_s	ϕ_s	E	σ_y	E_{tan}
Cellulose 3wt%	45	1500	0.03	12	0.35	8
Cellulose 5wt%	75	1500	0.05	12	0.35	8
Polyethylene	120	950	0.13	0.2	0.01	0.1
	138	950	0.15	0.2	0.01	0.1
AlMg1Si0.6	650	2670	0.25	70	0.75	12
AlMg1Si10	650	2670	0.25	70	0.35	5

Units: ρ_e and ρ_s are in kg/m^3, and E, σ_y, and E_{tan} are in GPa.

3.2. Representativeness of RVE

In general, the RVE size should be large enough that any increase in its volume is equally representative. On the other hand, minimizing the RVE size is desired to make simulations more computationally efficient. Therefore, the representativeness of an RVE is studied based on the microstructural properties and the resulting effective mechanical properties. For this purpose, the statistical descriptors of the PSD, such as mean pore-width and pore-size range, are analyzed across different RVE sizes. In addition, the CWD and effective macroscopic properties are also evaluated accordingly. Based on this study, the most favorable RVE size is selected. Thus, RVEs with 250, 500, 1000, 2000 and 3000 cells, are generated based on a symmetric and a right-skewed beta PDF and a constant solid fraction of 0.05. The corresponding statistical descriptors of the PSD of the structures are compared as shown in Fig. 5(a) &(c).

For the symmetric beta PDF (see Fig. 5(a)), with increasing number of cells from 250 to 3000, the pore-width range changes from 21.32–84.82 nm to 18.86–91.42 nm, while resulting in a constant mean pore-width of 53.27±0.02 nm. For the right-skewed beta PDF (see Fig. 5(c)), the pore-width range changes from 10.62–45.69 nm to 9.2–65.26 nm in this case, but the calculated average CWD remains the same regardless of the RVE size (refer to inner plot in Fig. 5(a) &(c)). The variation in the elastic and inelastic response in Fig. 5(d) is due to the 20% increase in the maximum pore-width (see Fig. 5(c)). From Fig. 5(b) &(d), it is clear that the effective macroscopic response is identical for converged statistical properties. Therefore, for the same solid fraction and mean pore-size, as well as the same CWD, the minimal representative size of the RVE is identified.

3.3. Influence of CWD

The average CWD for different pore-sizes in the structure, determined using both CD and DD approaches (as explained in Section 2.2.1), following reference PDF and solid fraction, is illustrated in Fig. 5(e). In the DD approach, the CWD varies with the pore size, whereas a constant CWD is defined to the entire structure in the CD approach.

The bulk response of the structure with CWD, as determined using both approaches, shows similar bulk elastic modulus (E) and plastic collapse stress (σ_{pl}), but differs significantly beyond σ_{pl}, as shown in Fig. 5(f). In particular, larger pore widths result in smaller CWD in the CD approach, leading to stronger stress softening compared to the DD approach (see Fig. 5(f)), as larger cells begin to deform earlier under small strains. Furthermore, densification occurs earlier in the CD
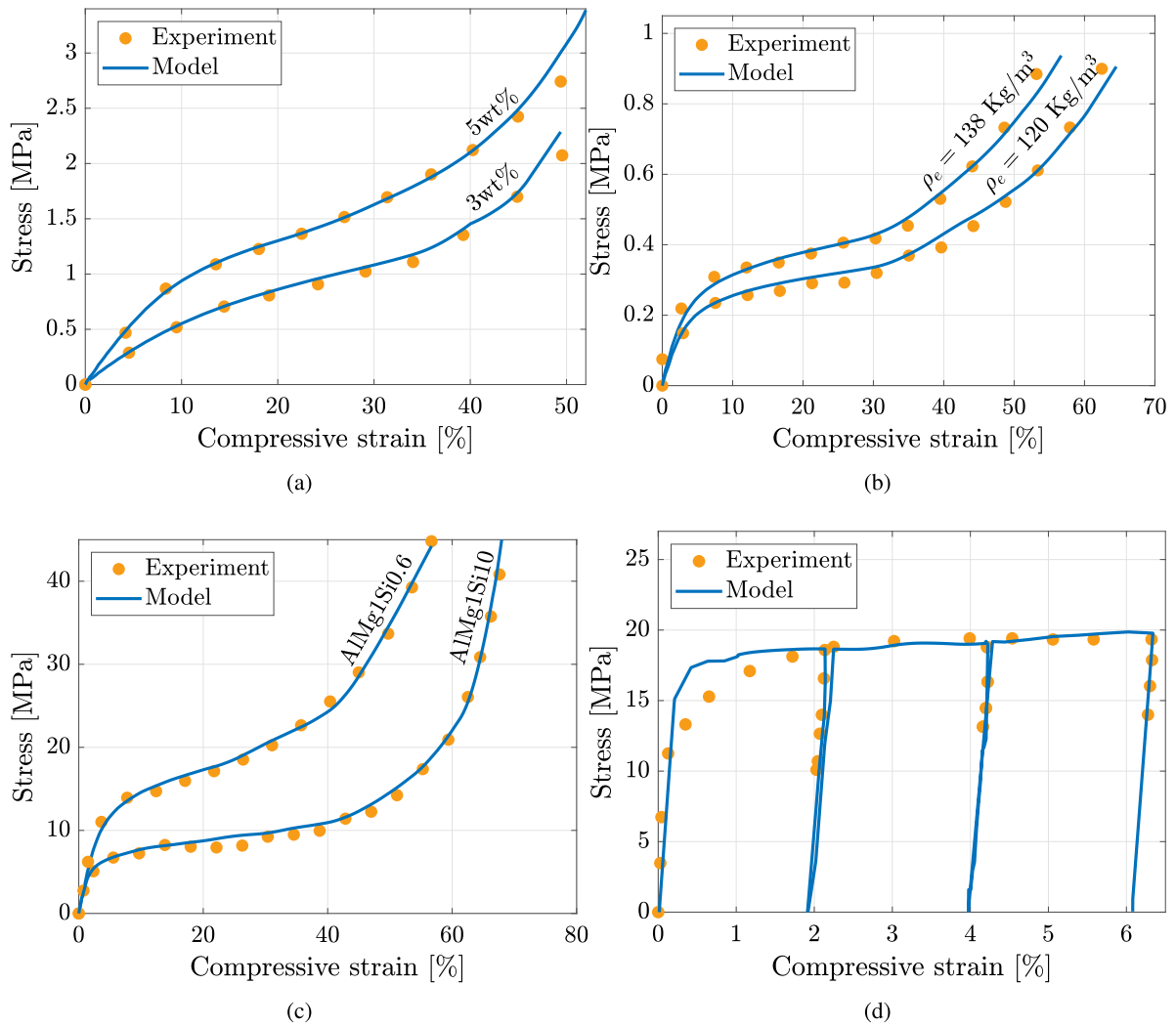
Fig. 4. Model validation against experimental results of (a) Cellulose aerogels, (b) polyethylene foams, (c) aluminium alloy foams, and (d) the cyclic response of AlMgSi0.6 with $\phi_s = 0.28$, under compression.

Table 2
Properties of the microstructure following the reference PDF with different CWD.

CWD (nm)	ϕ_s	E (MPa)	σ_y (MPa)	SEA (kJ/kg)
4.0	0.032	02.86	0.15	08.47
4.5	0.040	04.42	0.20	12.74
5.0	0.050	06.42	0.28	18.34
5.5	0.060	08.92	0.40	25.30
6.0	0.071	12.00	0.51	34.05

approach because smaller cells have larger CWDs, causing the cell walls to contact earlier after pore collapse. Accordingly, the densification is more strongly influenced by the smaller cells. Therefore, although the porosity of the structure remains the same, the CWD definition influences the bulk response.

The influence of the constant CWD on the bulk response of the structure is shown in Fig. 5(g). Accordingly, the solid fraction (ϕ_s) increases with CWD, resulting in reduced porosity and stiffening of the mechanical response. This trend is evident in Fig. 5(h) and (i), which illustrate the variations in E, σ_{pl} and specific energy absorption (SEA) with ϕ_s (refer Table 2). Specifically, increasing CWD leads to higher E, σ_{pl}, and SEA (Goods et al., 1997), while shortening the span of plateau regime and lowering the strain at which the densification begins. These effects are consistent with previous studies (Rege, 2021). Note that the

residual deformation exhibits only a minor variation with increasing CWD. Furthermore, the relationship between E and ϕ_s follows a scaling law with an exponent of approximately 1.8, which is close to the theoretical value of 2 predicted for open-cell foams (Gibson and Ashby, 1999). Similarly, σ_{pl} scales with ϕ_s with an exponent of 1.48, consistent with the findings by Gibson and Ashby (1999).

3.4. Influence of PSD

The PSD can vary based on different PDFs, each characterized by different statistical properties, such as the mean and standard deviation. It is important to study the influence of the PSD on the geometric parameters, such as solid fraction and CWD, as well as the bulk mechanical response of the structure.

3.4.1. Varying mean pore-width

For a given distribution with a constant standard deviation, the shape of the PSD remains unchanged. In this study, PSDs with constant standard deviation and varying mean pore widths (40, 50, 60, and 70 nm) are compared using a normal distribution, as shown in Fig. 6(a).

Due to the symmetric nature of the normal PDF, the PSDs are also symmetric and have a similar shape. However, the pore-width range (minimal and maximal values) shifts according to the selected mean pore-width. As a consequence, the resulting CWD (for a given
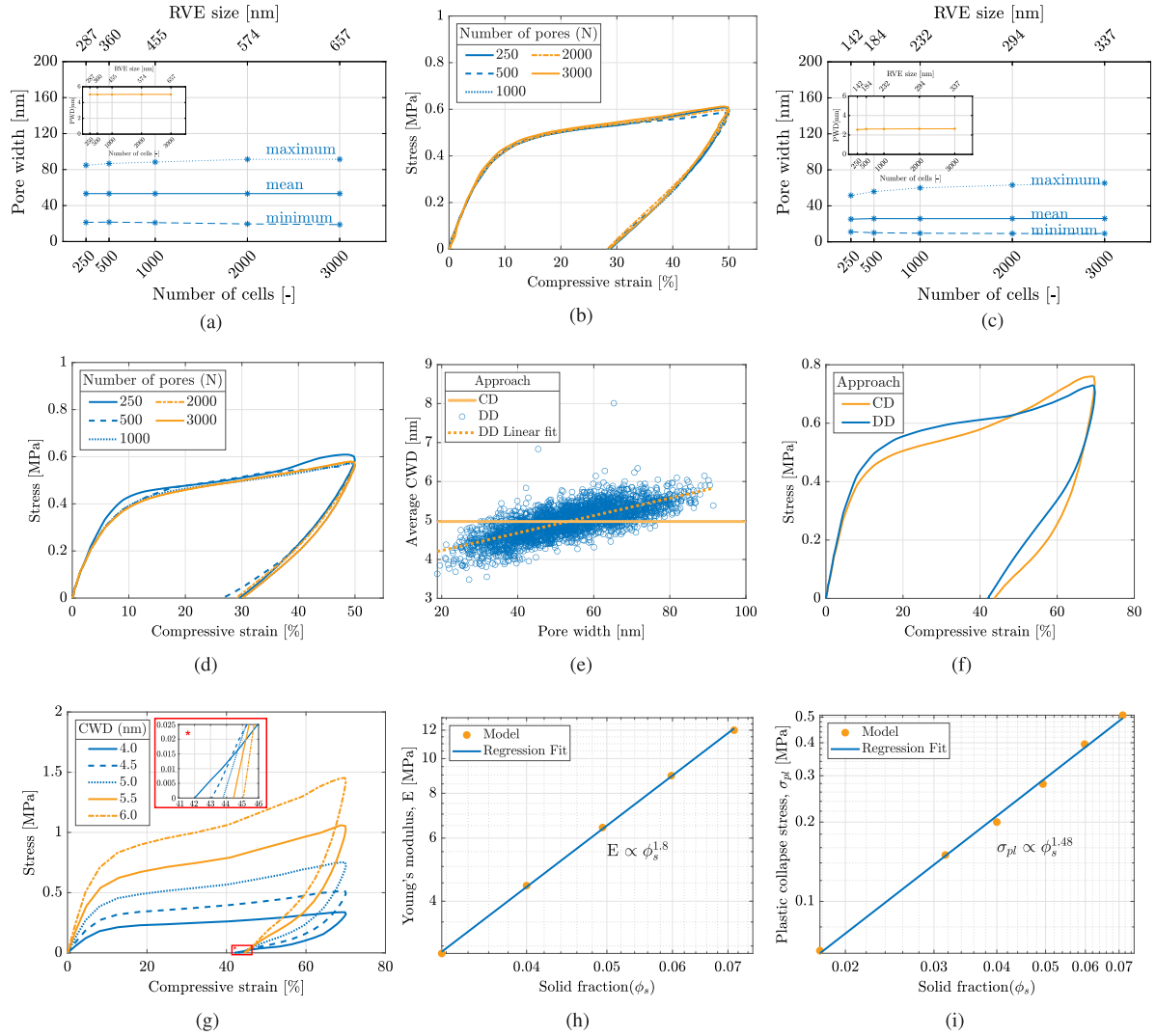
Fig. 5. Convergence study on the RVE size: (a) Pore-width with the average CWD in the subplot and (b) corresponding macroscopic response for symmetric beta PDF ($\alpha = 5$, $\beta = 5$), (c) pore-width with the average CWD in the subplot and (d) resulting macroscopic response for right-skewed beta PDF ($\alpha = 2$, $\beta = 10$). Comparison of CD and DD approach: (e) average CWD for each pore-width, and (f) bulk response of the structures. Influence of CWD and ϕ_S: (g) Bulk response (h) bulk stiffness and (i) plastic collapse stress of the microstructure subjected to compression.

Table 3
Properties of the structures with PSDs in Fig. 6(a), where the standard deviation and number of cells (N=1000) are held constant.

Pore Width[a]			Constant	RVE	E	SEA
Mean	Min.	Max.	CWD[a,b]	size[a]	(MPa)	(kJ/kg)
40	22	58	3.615	332	7.07	11.20
50	32	68	4.462	410	7.10	11.19
60	42	78	5.315	490	7.15	11.22
70	52	88	6.175	570	7.12	11.25

[a] Unit of all the parameters is nm.
[b] A constant CWD is determined for all structures with a constant solid fraction of 0.05.

Table 4
Properties of the structures with PSDs corresponding to Fig. 6(e), where the mean pore-width and number of cells (N=1000) are held constant.

SD	Pore Width[a]		Constant	RVE	E	SEA
	Min.	Max.	CWD[a,b]	Size[a]	(MPa)	(kJ/kg)
10	26	81	4.82	440	6.60	11.44
15	21	88	5.03	455	6.55	10.85
20	17	98	5.49	490	6.52	10.41

[a] Unit of all the parameters is nm.
[b] A constant CWD is determined for all structures with a constant solid fraction of 0.05.

solid fraction of 0.05) and RVE size increase proportionally with the mean pore-width (refer Table 3). The bulk responses of the structures under compressive loading and unloading are found to be similar, as illustrated in Fig. 6(c). The macroscopic properties, E ($\approx$ 7.11 MPa), σ_{pl} ($\approx$ 0.3 MPa) and SEA ($\approx$ 11.22 kJ/kg), remain consistent across all distributions. This is because the PSDs are identical when normalized, as shown in Fig. 6(b), resulting in the same CWD and RVE size. Consequently, the geometric properties scale with pore-width, resulting in similar bulk responses for structures with the same PSD shape and solid

fraction. This behavior extends the findings of Aney and Rege (Aney and Rege, 2023), who demonstrated similar results in the linear elastic regime, to larger deformations.

3.4.2. Varying shape of PSD

Different PSDs with constant mean pore-width and different standard deviation (SD) are investigated using a symmetric beta PDF. The PDFs with $\alpha = \beta = 10$, 5, and 2, having SD = 10, 15, and 20, respectively, and a constant mean pore-width of 53 nm, are shown
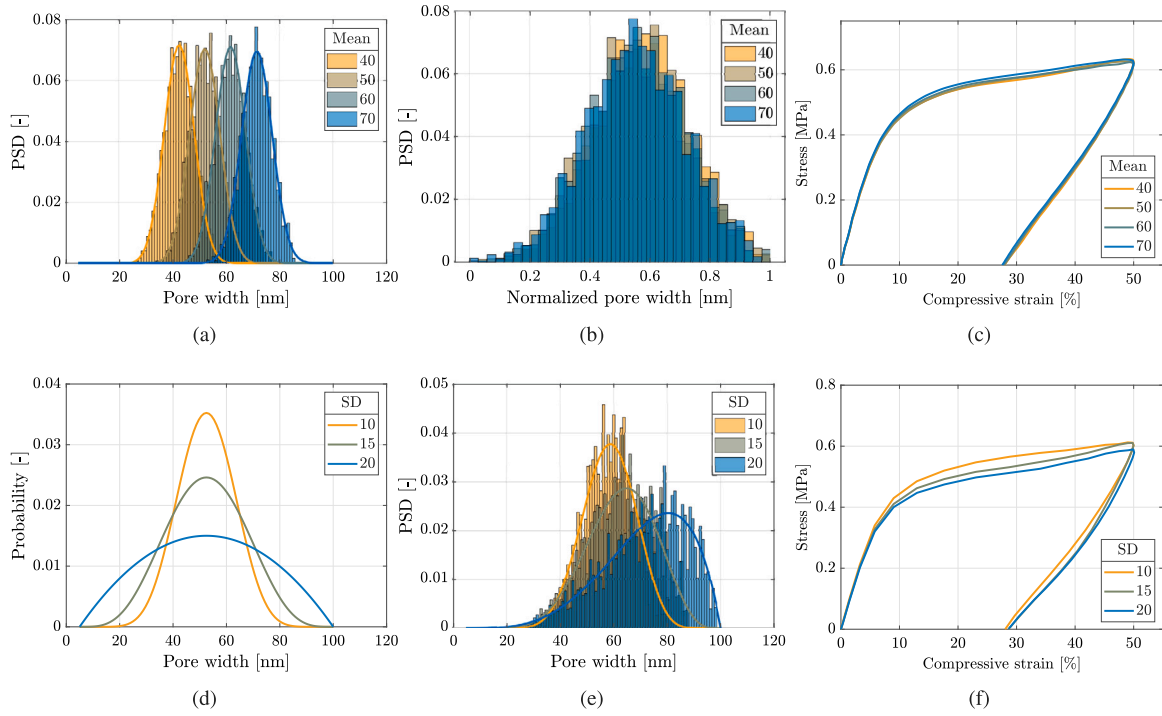
Fig. 6. Comparison of (a) PSDs based on normal PDFs and (b) PSDs with pore-widths in normalized scale with different mean pore-widths and constant SD, (c) bulk responses of microstructures with PSDs shown in (a), comparison of (d) beta PDFs and (e) PSDs corresponding to the PDFs with varying SD and constant mean pore-width, and (f) bulk responses of microstructures with PSDs from (e).

in Fig. 6(d). The corresponding PSDs of the Voronoi structures are depicted in Fig. 6(e) in comparison with the desired PSDs corresponding to the PDFs in Fig. 6(d). As the standard deviation increases, the pore-width range expands (refer Table 4), leading to a variation in the shape of the PSDs. As a consequence, marginal differences in the bulk response of the structures are observed beyond the elastic regime (refer to Fig. 6(f)). E in the elastic regime and σ_{pl} remain identical, as they share the same solid fraction. However, beyond the elastic regime, softening response is observed as the standard deviation of the PDF increases, despite an increase in the CWD. This behavior is attributed to the shift in the PSD shape, where larger cells dominate more, deforming earlier and contributing to the observed response. Note that the SEA decreases with increasing SD (refer Table 4) and no significant change is observed in the residual deformation during unloading.

3.4.3. Varying PSD with constant CWD

To study only the influence of the PSD, neglecting the effect of the CWD on the bulk response, we compare here different PSDs using normal and beta PDFs (denoted as PSD-1, 2 & 3) that result in a structure with the same average CWD and solid fraction. The statistical parameters of the three different PDFs, along with the corresponding geometric properties of the resulting structures, are detailed in Table 5. The PSDs and their corresponding cumulative PSDs are shown in Fig. 7(a) &(b). All structures have an RVE size of 400 ± 10 nm, with varying pore-width ranges, mean pore-widths, and standard deviations (SDs), while maintaining an average CWD of 4.5 nm and a solid fraction of 0.05.

The bulk mechanical response of these structures, depicted in Fig. 7(c) & (d), exhibits noticeable differences. While the stiffness ($E \approx$ 6 MPa) and the plastic collapse stress ($\sigma_y \approx 0.3$ MPa) remain unaffected by all PSDs, variations in the plateau stress and the densification behavior are observed. A detailed comparison of the PDFs and their statistical properties indicates that structures with smaller mean pore-widths tend to exhibit reduced plateau stress, contradicting previous findings by Aney and Rege (Aney and Rege, 2023). However, an examination of the cumulative PSDs in Fig. 7(b) reveals that PSD-3, despite of a smaller

Table 5
Geometric properties of the structures with PSDs corresponding to Fig. 7(a), and the same average CWD of 4.5 nm and solid fraction of 0.05 with N=1000 cells.

PSD		Pore width[1]			SD	RVE
No.	Input	Mean	Min.	Max.		Size[a]
1	Normal (μ=50, s=7)	50	33	68	5.8	410
2	Beta (α=17.6, β=20)	50	28	70	7.3	410
3	Normal (μ=40, s=21)	45	14	90	15	390

[a] Unit of all the parameters is nm.

mean pore-width, includes a higher volume fraction of larger pores compared to PSD-1 and PSD-2. This results in a softened response for PSD-3 beyond 10% strain due to the deformation of larger cells. In addition, the greater volume contribution of smaller pores below the mean pore-width in PSD-3 leads to earlier densification compared to PSD-1 and PSD-2. Although PSD-1 and PSD-2 have identical mean pore widths, the different shapes of their PSDs — due to the varying standard deviations — significantly affect the bulk response at strains above 10%. However, their effects on SEA ($\approx$ 22 kJ/kg) and permanent set during unloading remain minimal.

4. Discussion

The computational model representing the realistic pore morphology of porous materials and capturing the important structural properties (PSD, solid fraction and pore wall thickness) is generated using RCPPS and LVT (Chandrasekaran et al., 2021). The pore morphology of the model is described by the PSD, which can be derived from the given PDF as outlined in Section 2.1. The average CWD of the structure is computed for a given solid fraction. Accordingly, RVEs of different sizes that inherit the full range of the PSD exhibit similar bulk responses. The smallest RVE size is identified through a convergence study of
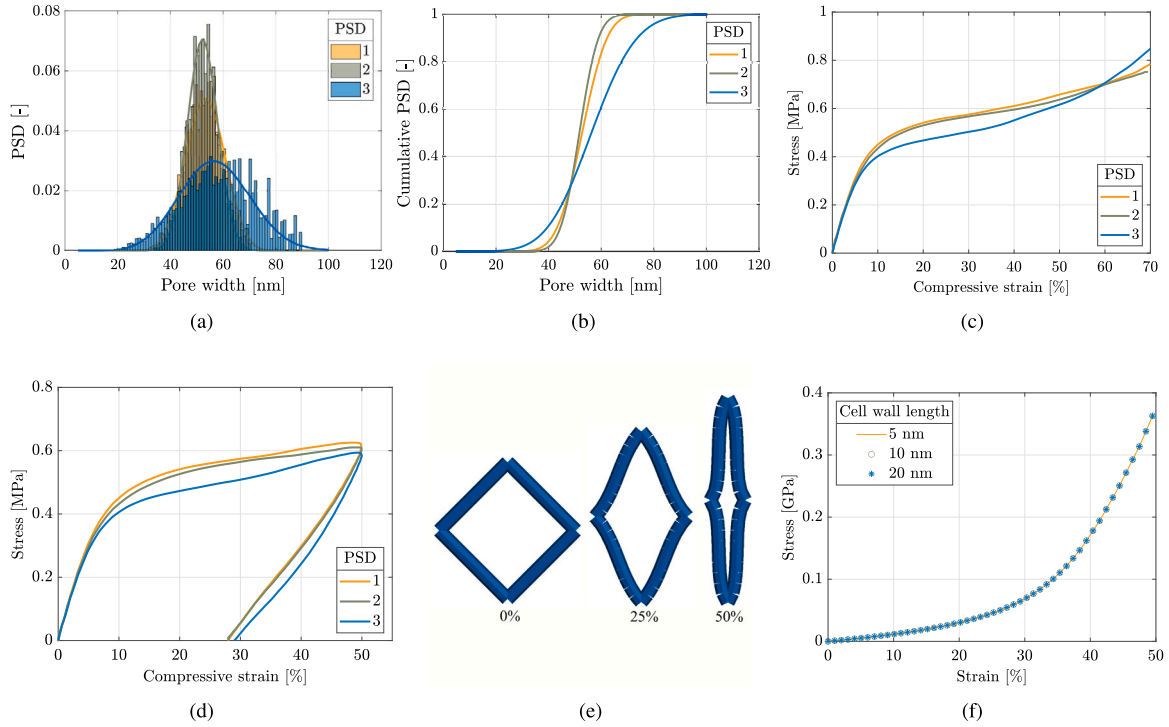
Fig. 7. Comparison of (a) PSDs and (b) cumulative PSDs of microstructure with similar CWD and different SD, bulk response of the corresponding microstructures under (c) monotonic and (d) cyclic compression loading, (e) cell wall behavior of a square-shaped unit cell subjected to tension along its diagonal at 0%, 25% and 50% strain, and (f) the corresponding stress–strain response for different cell sizes.

Table 6
Geometric properties of square shaped cell with cell wall length (l) and the same solid fraction.

Cell wall length (l) (nm)	Cell width ($\sqrt{2}l$) (nm)	CWD (d_f) (nm)
5	7.07	0.73
10	14.14	1.46
20	28.28	2.92

the effective geometric and mechanical properties of the structure. The computational model effectively captures both elastic and inelastic behavior typical for porous materials. The bulk elastic modulus and plastic collapse stress of the RVE scale with the solid fraction, exhibiting scaling exponents of 1.8 and 1.5, respectively. These exponents agree well with the results of Gibson and Ashby (1982). The solid fraction significantly influences the SEA and permanent set under cyclic loading. In fact, the CWD and elastic modulus increase with the solid fraction while decreasing the plateau regime and the compressive strain at which densification occurs. The solid fraction is a dimensionless quantity and can be conveniently used as a model parameter, allowing the CWD to be calculated for a given RVE size by reverse engineering as demonstrated in Chandrasekaran et al. (2021). In addition, the method used to define the CWD — whether through the CD or DD approach — also impacts the overall bulk response. Therefore, further experimental investigation is needed to explore the true distribution of CWD in real porous structures. For a constant solid fraction and PSD with the same shape, the bulk response of the structure remains similar at different scales. This is because the average CWD and RVE sizes scale proportionally with the given pore-width interval and solid fraction. This could be better explained with an example of an idealized square-shaped cell, as first proposed in Rege et al. (2016).

For illustration we consider a square shape cell with different side lengths (l = 5, 10 and 20 nm), but the same solid fraction. The corresponding CWD (d_f) with a circular cross-section are listed in Table 6. Note that for a given solid fraction, the CWD is proportional

to the cell width (diagonal of the square cell). The normal stress σ in a square cell subjected to tension along its diagonal (Rege and Itskov, 2018) can be expressed as

$$\sigma(\lambda, l) = E(\lambda - 1)\sin\varphi \left[\sin\varphi + \frac{3\cos\varphi d_f}{2l}\right], \tag{8}$$

where λ represents the stretch along the diagonal, l is the side length, φ is the angle of a single cell wall relative to the horizontal axis, d_f is the cross-sectional CWD. Since both d_f and l scale proportionally (as shown in Table 6), the ratio d_f/l remains constant, resulting in the same normal stress for square cells of different sizes but the same solid fraction and pore shape. To see the response of the square cell at high strains, a FE simulation is carried out with a linear elastic material. Fig. 7(e) shows the deformation behavior of a square-shaped cell subjected to tension along its diagonal direction. From Fig. 7(f), we can see that even at higher strains, the structure shows a similar response.

In contrast, the structure with a different PSD, but the same average CWD and solid fraction, significantly affects the bulk response. From the cumulative PSDs and corresponding bulk responses, it is inferred that the plateau regime in the stress–strain curve are influenced by larger cells, while the densification behavior is governed by smaller cells. This observation is consistent with the findings by Rege et al. (2016) regarding the collapse of cells. For a given solid fraction, the PSD has a minimal effect on SEA and permanent set.

5. Conclusion

In this study, the influence of various structural parameters, such as PSD, solid fraction, and pore wall thickness, on the elastic and inelastic behavior of cellular-like open-porous materials has been investigated through a detailed computational modeling approach. For a better understanding of the structure–property relationship, it is crucial to focus on the PSD, rather than just the PDF. The results highlight that the PSD and the solid fraction are the most significant geometric features that determine the bulk mechanical response.

The findings confirm that the solid fraction primarily dictates the elastic modulus and plastic collapse stress, in accordance with established scaling laws. Furthermore, notable effects on the specific energy absorption and residual deformation under cyclic loading were observed. In contrast, the PSD plays a critical role in shaping the nonlinear deformation behavior, particularly the plateau and densification regimes. Note also that both PSD and solid fraction are dimensionless quantities and therefore remain consistent across different length scales (from nano- to macroscale). On the other hand, dimensional parameters such as the CWD and RVE size are scale-dependent and derived from the PSD and solid fraction, making them secondary descriptors of the structural performance.

When attempting to correlate the synthesis parameters with material performance, it is essential to consider both PSD and solid fraction. Although the computational framework in this study is based on randomly shaped pores and cylindrical pore wall cross-sections, the insights gained are not limited to this geometry. Thus, while the study focuses on a specific configuration, it provides a broader understanding of the relationship between structural parameters and material behavior that can be applied to other types of open-porous materials.

CRediT authorship contribution statement

Rajesh Chandrasekaran: Writing – original draft, Visualization, Validation, Software, Resources, Methodology, Investigation, Formal analysis, Conceptualization. **Mikhail Itskov:** Writing – review & editing, Supervision. **Ameya Rege:** Writing – review & editing, Supervision, Formal analysis.

Declaration of competing interest

The authors declare that they have no known competing financial interests or personal relationships that could have appeared to influence the work reported in this paper.

Data availability

The authors are unable or have chosen not to specify which data has been used.

References

Aney, S., Rege, A., 2023. The effect of pore sizes on the elastic behaviour of open-porous cellular materials. Math. Mech. Solids 28 (7), 1624–1634.

Aney, S., Rege, A., 2025. Network decomposition model to describe the solid and gaseous thermal conductivity in open-porous (nano) materials. Int. J. Heat Mass Transfer 236, 126316.

Ates, M., Karadag, S., Eker, A.A., Eker, B., 2022. Polyurethane foam materials and their industrial applications. Polym. Int. 71 (10), 1157–1163.

Bennett, T.D., Coudert, F.-X., James, S.L., Cooper, A.I., 2021. The changing state of porous materials. Nat. Mater. 20 (9), 1179–1187.

Cai, G., Yan, P., Zhang, L., Zhou, H.-C., Jiang, H.-L., 2021. Metal–organic framework-based hierarchically porous materials: synthesis and applications. Chem. Rev. 121 (20), 12278–12326.

Chandrasekaran, R., Hillgärtner, M., Ganesan, K., Milow, B., Itskov, M., Rege, A., 2021. Computational design of biopolymer aerogels and predictive modelling of their nanostructure and mechanical behaviour. Sci. Rep. 11 (1), 1–10.

Davis, M.E., 2002. Ordered porous materials for emerging applications. Nature 417 (6891), 813–821.

Ghosh, S., Moorthy, S., 2004. Three dimensional voronoi cell finite element model for microstructures with ellipsoidal heterogeneties. Comput. Mech. 34, 510–531.

Gibson, I., Ashby, M.F., 1982. The mechanics of three-dimensional cellular materials. Proc. R. Soc. A 382 (1782), 43–59.

Gibson, L.J., Ashby, M.F., 1999. Cellular Solids: Structure and Properties, second ed. Cambridge University Press, Cambridge, p. 510.

Gibson, L.J., Ashby, M.F., Schajer, G., Robertson, C., 1982. The mechanics of two-dimensional cellular materials. Proc. R. Soc. A 382 (1782), 25–42.

Goods, S., Neuschwanger, C., Henderson, C., Skala, D., 1997. Mechanical properties and energy absorption characteristics of a polyurethane foam. In: SAND97-8490. Sandia National Laboratories, p. 43.

Jin, F.-L., Zhao, M., Park, M., Park, S.-J., 2019. Recent trends of foaming in polymer processing: A review. Polymers 11 (6), 953.

Jones, D.R., Ashby, M.F., 2018. Engineering materials 1: An introduction to properties, applications and design. Butterworth-Heinemann.

Kelly, A., 2006. Why engineer porous materials? Philos. Trans. R. Soc. A: Math. Phys. Eng. Sci. 364 (1838), 5–14.

Kraynik, A.M., 2006. The structure of random foam. Adv. Eng. Mater. 8 (9), 900–906.

McCullough, K.Y., Fleck, N.A., Ashby, M.F., 1999. Uniaxial stress–strain behaviour of aluminium alloy foams. Acta Mater. 47 (8), 2323–2330.

Merillas, B., Vareda, J.P., Martín-de León, J., Rodríguez-Pérez, M.Á., Durães, L., 2022. Thermal conductivity of nanoporous materials: where is the limit? Polymers 14 (13), 2556.

Polarz, S., Smarsly, B., 2002. Nanoporous materials. J. Nanosci. Nanotechnol. 2 (6), 581–612.

Rechberger, F., Niederberger, M., 2017. Synthesis of aerogels: from molecular routes to 3-dimensional nanoparticle assembly. Nanoscale Horizons 2 (1), 6–30.

Rege, A., 2021. Constitutive modeling of the densification behavior in open-porous cellular solids. Materials 14 (11), 2731.

Rege, A., Aney, S., Milow, B., 2021. Influence of pore-size distributions and pore-wall mechanics on the mechanical behavior of cellular solids like aerogels. Phys. Rev. E 103 (4), 043001.

Rege, A., Itskov, M., 2018. A microcell-based constitutive modeling of cellulose aerogels under tension. Acta Mech. 229, 585–593.

Rege, A., Preibisch, I., Schestakow, M., Ganesan, K., Gurikov, P., Milow, B., Smirnova, I., Itskov, M., 2018. Correlating synthesis parameters to morphological entities: Predictive modeling of biopolymer aerogels. Materials 11 (9), 1670.

Rege, A., Schestakow, M., Karadagli, I., Ratke, L., Itskov, M., 2016. Micro-mechanical modelling of cellulose aerogels from molten salt hydrates. Soft Matter 12 (34), 7079–7088.

Santos-Rosales, V., Alvarez-Rivera, G., Hillgärtner, M., Cifuentes, A., Itskov, M., García-González, C.A., Rege, A., 2020. Stability studies of starch aerogel formulations for biomedical applications. Biomacromolecules 21 (12), 5336–5344.

Sharma, V., Grujovic, N., Zivic, F., Slavkovic, V., 2019. Influence of porosity on the mechanical behavior during uniaxial compressive testing on voronoi-based open-cell aluminium foam. Materials 12 (7), 1041.

Smith, B., Szyniszewski, S., Hajjar, J., Schafer, B., Arwade, S., 2012. Steel foam for structures: A review of applications, manufacturing and material properties. J. Constr. Steel Res. 71, 1–10.

Sotomayor, O.E., Tippur, H.V., 2014. Role of cell regularity and relative density on elastoplastic compression response of 3-D open-cell foam core sandwich structure generated using voronoi diagrams. Acta Mater. 78, 301–313.

Thommes, M., Schlumberger, C., 2021. Characterization of nanoporous materials. Annu. Rev. Chem. Biomol. Eng. 12 (1), 137–162.

Yang, X.-Y., Chen, L.-H., Li, Y., Rooke, J.C., Sanchez, C., Su, B.-L., 2017. Hierarchically porous materials: synthesis strategies and structure design. Chem. Soc. Rev. 46 (2), 481–558.

Zhao, S., Malfait, W.J., Guerrero-Alburquerque, N., Koebel, M.M., Nyström, G., 2018. Biopolymer aerogels and foams: Chemistry, properties, and applications. Angew. Chem. Int. Ed. 57 (26), 7580–7608.